materials

MDPI

Article

Template-Engineered Flexible PZT/PDMS Composites for High-Output Piezoelectric Sensing and Spatially Resolved Mechanical Detection

Sihao Jia, Xiufang Yuan, Jing Xu, Mao Li and Changhong Yang *

Shandong Provincial Key Laboratory of Green and Intelligent Building Materials, University of Jinan, Jinan 250022, China
* Correspondence: mse_yangch@ujn.edu.cn

Abstract

Flexible piezoelectric sensors are promising for wearable electronics, but simultaneously achieving high piezoelectric output and mechanical flexibility remains challenging. Here, we report a flexible PZT/PDMS composite film fabricated using dust-free paper as a three-dimensional template to establish a continuous PZT ceramic network, followed by PDMS infiltration to impart flexibility and structural integrity. The composite exhibits a high piezoelectric coefficient (d_{33}) of approximately 34 pC/N, generating an output voltage of up to 28 V under mechanical impact. The device also demonstrates a rapid dynamic response and stable electrical output over repeated loading cycles of 10^6. Furthermore, a 3 × 3 electrode array enables spatially resolved detection of mechanical stimuli across the continuous composite film, with distinct voltage responses from individual sensing regions. Demonstrations involving finger pressing, hand tapping, hammer impact, foot stepping, keyboard typing, and water-flow monitoring further highlight its versatility in detecting diverse mechanical disturbances. This work establishes a template-assisted fabrication strategy for flexible ceramic-polymer piezoelectric composites and demonstrates their potential for spatially resolved mechanical sensing in wearable and human–machine interface applications.

Keywords: PZT/PDMS composite; flexible piezoelectric film; piezoelectric sensing; wearable electronics; interconnected piezoceramic skeleton

1. Introduction

Flexible pressure sensors have attracted significant attention in advanced intelligent sensing systems, particularly for wearable electronics and human–machine interaction, owing to their efficient electromechanical transduction [1–4]. Featuring exceptional mechanical compliance, these devices can seamlessly conform to human skin or organs, enabling non-invasive, continuous, and high-fidelity monitoring of physiological signals [5,6]. However, long-term wearable applications require not only mechanical compliance but also sustainable and autonomous power sources. This has spurred extensive efforts to develop flexible devices that integrate mechanical compliance with energy-harvesting capabilities. Among various self-powered approaches, piezoelectric flexible sensors have emerged as a promising platform because they can directly convert mechanical stimuli into electrical signals while harvesting energy from biomechanical motions, enabling continuous self-powered sensing [7,8].

Check for updates

Academic Editor: Haim Abramovich

Received: 19 October 2026
Revised: 22 November 2026
Accepted: 24 November 2026
Published: 27 November 2026

Copyright: © 2026 by the authors. Licensee MDPI, Basel, Switzerland. This article is an open access article distributed under the terms and conditions of the Creative Commons Attribution (CC BY) license.

Current strategies for developing flexible piezoelectric sensors (FPSs) can be broadly categorized into three representative approaches: piezoelectric polymers, such as poly (vinylidene fluoride) (PVDF) and its copolymers; ultrathin piezoelectric ceramic films integrated with flexible substrates, such as mica; and ceramic/polymer composites [9–12]. While piezoelectric polymers offer excellent mechanical flexibility and biocompatibility, their intrinsically low piezoelectric coefficients (d_{33}) constrain the achievable electrical output [13]. Piezoelectric ceramic films integrated with flexible substrates retain the high piezoelectric activity of inorganic materials; however, their limited mechanical compliance substantially restricts their practical applicability, with a typical bendable angle of less than 90° [14]. In contrast, incorporating inorganic piezoelectric fillers into flexible polymer matrices provides an attractive strategy for reconciling high piezoelectric performance with mechanical compliance [15]. In these systems, the inorganic phase primarily governs the electromechanical performance, whereas the polymer matrix accommodates large deformations. Based on the geometry of the inorganic phase, these piezoelectric composites are classified into 0–3, 1–3, and 3–3 connectivity structures [16,17]. Although 0–3 composites exhibit excellent flexibility, the significant stiffness mismatch and the discontinuous distribution of the piezoelectric phase severely hinder mechanical load transfer among the ceramic fillers, thereby preventing them from fully exploiting their intrinsic piezoelectric potential [18,19]. While 1–3 composites enhance longitudinal stress transfer efficiency, the non-continuous nature of the transverse inorganic phase makes them prone to hysteresis and fatigue under high stress; moreover, their complex fabrication processes limit their practical application in real-world devices [20,21].

Therefore, continuous and interconnected piezoceramic skeleton-based composites (3–3) have emerged as an effective strategy for simultaneously improving the flexibility and piezoelectric performance of flexible devices [22–28]. This continuous three-dimensional (3D) framework overcomes the limitations associated with the isolated and discontinuous piezoelectric phases in conventional particulate composites. By establishing continuous percolation pathways, the 3D ceramic network facilitates efficient stress transfer among interconnected ceramic domains while promoting electrical signal collection, thereby reconciling high piezoelectric activity with mechanical compliance. Among these approaches, sacrificial templating has emerged as a promising strategy owing to its facile processing and ability to construct well-defined, 3D interconnected architectures [24,26]. Previous studies have demonstrated that interconnected piezoceramic frameworks can improve stress transfer and help combine ceramic piezoelectric activity with the flexibility of polymer-based devices. However, high-temperature sintering can induce substantial shrinkage and shape distortion, complicating the large-area and high-quality ceramic skeleton fabrication [29]. This bottleneck poses a major barrier to their integration into large-area flexible devices, such as sensing arrays [30–32]. This bottleneck has severely impeded their integration into large-area, high-performance flexible devices, such as sensing arrays constructed on three-dimensionally interconnected ceramic composite substrates.

To overcome these challenges, we develop a flexible piezoelectric sensor (FPS) featuring a 3D-interconnected $PbZr_{0.52}Ti_{0.48}O_3$ (PZT)-skeleton/polydimethylsiloxane (PDMS) composite as a piezoelectric functional layer. Through the integration of a sacrificial templating strategy with mold-assisted sintering, a large-area, continuous 3D PZT skeleton was constructed and subsequently embedded in a PDMS matrix to obtain a composite film measuring approximately 4.5 × 4.5 cm^2. Enabled by efficient stress transfer throughout the continuous ceramic network, the resulting device delivers a robust piezoelectric response (a d_{33} of 34 pC/N and an output voltage of 28 V), along with mechanical durability under repeated loading. In practical demonstrations, the sensor enables pressure sensing under wearable conditions and supports spatially resolved mechanical detection through a 3 ×

3 electrode array on the same continuous composite film. This scalable and continuous piezoceramic architecture provides a promising platform for high-performance flexible electronics and spatial pressure mapping.

2. Experimental Section

2.1. Synthesis of the PZT Precursor Solution

The lead zirconate titanate (PZT) precursor solution was prepared via a sol–gel method. First, tetrabutyl titanate ($C_{16}H_{36}O_4Ti$, 98%, Aladdin, Shanghai, China) and acetylacetone ($C_5H_8O_2$, 99.95%, Macklin, Shanghai, China) were mixed and kept under stirring at room temperature for 4 h to prepare Solution A. In parallel, lead (II) acetate trihydrate ($Pb(CH_3COO)_2{\cdot}3H_2O$, 99.0%, Sinopharm, Shanghai, China) was dissolved in 2-methoxyethanol at 60 °C under constant stirring, with glacial acetic acid (CH_3COOH, 99.8%, Sinopharm) added rapidly to aid dissolution. After complete dissolution, heating was stopped and the mixture was cooled to room temperature, yielding Solution B. Zirconium n-propoxide ($C_{12}H_{28}O_4Zr$, 70%, Aladdin, China) was then mixed with 2-methoxyethanol at room temperature to obtain Solution C. Subsequently, Solutions B and C were added to Solution A in sequence. The resulting mixture was stirred continuously for 12 h, ultimately producing a clear 0.4 mol/L $Pb_{1.1}Zr_{0.52}Ti_{0.48}O_3$ precursor solution.

2.2. Fabrication of Flexible Piezoelectric Sensor

The dust-free paper (Kimtech Pure W5, Kimberly-Clark Professional (Roswell, GA, USA), product codes 06179 [US] and 7659 [EU]), composed of 50% rayon and 50% polyester [33] and measuring approximately 5.0 cm × 5.0 cm, was immersed in the pre-prepared PZT precursor solution for 5 min and dried on an 80 °C hot plate for 5 min. This immersion–drying process was repeated five times to progressively deposit PZT precursors onto the supporting substrate. The dried precursor, measuring approximately 5.0 × 5.0 cm^2, was subsequently placed between two alumina ceramic sheets with a gap of 3 mm during sintering at 800 °C in a muffle furnace for 2 h, yielding a crystallized, 3D-interconnected PZT-based piezoelectric ceramic skeleton with a final measured size of 4.5 × 4.5 cm^2. Meanwhile, PDMS (SYLGARD^{TM} 184 Silicone Elastomer Base, Dow, Midland, MI, USA) and its corresponding curing agent were thoroughly mixed by stirring at a mass ratio of 10:1 [34]. The mixture was vacuum-degassed until the bubbles disappeared. After degassing, the as-prepared PDMS mixture was coated onto the PZT skeleton and allowed to infiltrate naturally, followed by curing on a hot plate at 80 °C for 30 min to obtain the PZT-skeleton/PDMS composite. The resulting composite had an average thickness of approximately 2.3 mm and a nominal ceramic mass fraction of 85 wt%. In the composite, the volume fractions of PZT and PDMS were determined to be 42 vol% and 58 vol%, respectively. For comparison, the sintered PZT skeleton was ground into powder and mixed with the as-prepared PDMS mixture at a volume ratio of 42: 58. Subsequently, the mixture was poured into a mold and cured on a hot plate at 80 °C for 30 min, yielding a composite with a thickness of approximately 2.3 mm, in which the PZT powder was randomly dispersed in the PDMS matrix (designated as PZT-powder/PDMS). The composite was assembled by attaching copper tape electrodes and lead wires to its opposing surfaces, followed by polyimide (PI) tape encapsulation. In addition, to construct the sensing array, a separate lead wire was connected to each electrode, and the assembly was then encapsulated with PI tape. The electrodes of each sensing unit were patterned to dimensions of 5 mm × 5 mm with an edge-to-edge spacing of 5 mm between adjacent units. Polarization of the composites was carried out in a 120 °C silicone oil bath under an electric field of 20 kV/cm for 3 h, ultimately yielding PZT/PDMS-based FPS.

2.3. Characterization and Instrumentation

The crystal structure of the PZT-based piezoceramic framework was characterized using a Bruker D8 X-ray diffractometer (XRD, Bruker AXS, Karlsruhe, Germany) with Cu Kα radiation (λ = 1.5406 Å) operated at 40 kV and 40 mA. The surface morphology and microstructure of the dust-free paper, dust-free paper/PZT precursor, PZT skeleton, and PZT/PDMS composite were characterized by scanning electron microscopy (SEM, GeminiSEM 360, Carl Zeiss, Oberkochen, Germany). d_{33} was measured using a quasi-static tester (ZJ-6A, Institute of Acoustics, CAS, Beijing, China). The electrical output of the PZT/PDMS device was measured using an oscilloscope (MDO34, Tektronix, Inc., Beaverton, OR, USA) with a passive voltage probe at 1× attenuation under various mechanical excitation conditions. The input channel was DC-coupled with a 1 MΩ input impedance. Waveforms were acquired at 2.5 GS/s using Peak Detect acquisition and Auto trigger mode. Its frequency-dependent response, load-dependent output, mechanical durability, impact response, and human-motion sensing performance were further evaluated. For long-term cyclic stability testing, an arbitrary waveform generator was used to drive a cyclic loading system (exciter 4808 and power amplifier 2719, Bruel & Kjær, Virum, Denmark) to apply periodic forces.

2.4. AI-Assisted Methods

The device schematic in Figure 1d was generated using ChatGPT's image-generation tool (OpenAI, San Francisco, CA, USA), accessed through ChatGPT 6 Sol, with a photograph of the assembled device as a reference. The following prompt specified the device architecture and electrical connections. "Create a 3D cutaway schematic of a flexible PZT/PDMS piezoelectric sensor in a gently bent configuration. Show an interconnected blue PZT/PDMS network between copper foil electrodes, with amber PI tape encapsulation. Attach red lead wires to the outward-facing copper surfaces using silver paste beneath the PI tape. Label PI tape, copper foil electrode, PZT/PDMS, silver paste, and lead wire. Use a white background and a clean scientific illustration style." The human-body schematic used to illustrate human-motion sensing was generated using ChatGPT (GPT-5.6 Sol, OpenAI) with the following prompt. Create a front-facing, full-body 3D illustration of an adult male standing upright with arms slightly away from the torso. Use a smooth, pale blue-gray surface with subtle anatomical definition and soft shading.

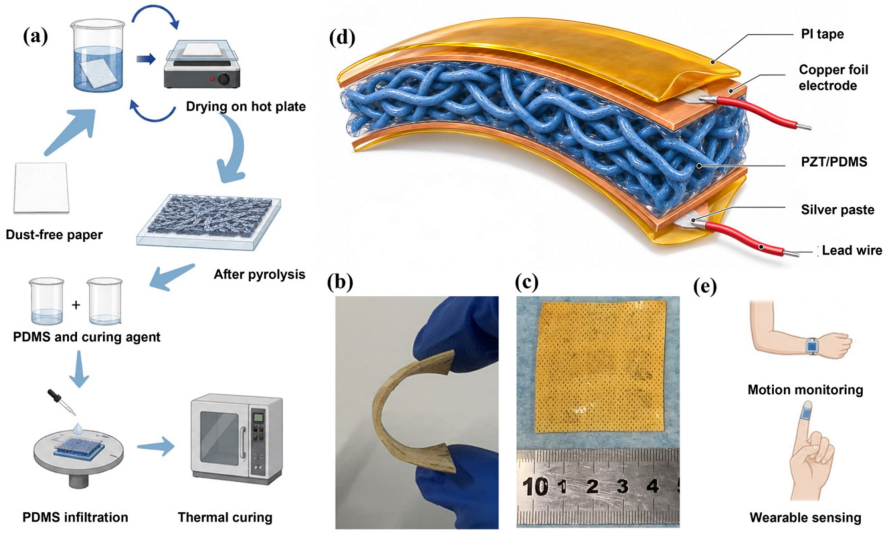

Figure 1. Design, fabrication, and application scenarios of the flexible pressure sensor. (**a**) Schematic illustration of the fabrication process of the PZT-skeleton/PDMS composite. (**b**) Photographs of the

fabricated PZT-skeleton/PDMS composite in manually bent states, and (**c**) after 1000 bending-release cycles. (**d**) Schematic diagram of the PZT-skeleton/PDMS-based FPS architecture. (**e**) Potential applications of the sensor in wearable, motion, pressure, and running sensing. The schematic in panel (**d**) was generated using ChatGPT's image-generation tool (OpenAI), accessed through ChatGPT 6 Sol, and reviewed and edited by the authors.

3. Results

3.1. Structural Design of the Flexible PZT-Skeleton/PDMS-Based FPS

Figure 1a illustrates the fabrication process of the flexible PZT-skeleton/PDMS piezoelectric composite. During the high-temperature sintering process, the dust-free paper template is completely removed via thermal decomposition into carbon dioxide and water vapor, ultimately forming an interconnected PZT-based piezoelectric ceramic skeleton. Subsequently, embedding this interconnected ceramic skeleton into a PDMS matrix endows the resulting composite with exceptional flexibility. Importantly, this PZT-skeleton/PDMS piezoelectric composite exhibits excellent flexibility and can withstand large bending deformations, as verified by Figure 1b. In addition, no obvious cracks were observed in the embedded ceramic skeleton even after 1000 cycles of bending deformation (Figure 1c), demonstrating its robust resistance to bending as well as reliable structural integrity. This composite was then integrated into the FPS as the piezoelectric active layer, and the corresponding device architecture is presented in Figure 1d. Benefiting from the synergistic integration of exceptional flexibility and high piezoelectric performance, the developed FPS demonstrates great potential for wearable electronics and healthcare monitoring (Figure 1e).

3.2. Microstructure Characterization

As shown in Figure 2a, the dust-free paper consists of randomly interwoven slender fibers that form a porous three-dimensional network, serving as a structural template for PZT deposition. Following repeated immersion in the PZT precursor solution and subsequent drying, a relatively uniform, uncrystallized PZT precursor was successfully coated on the fiber surfaces, as depicted in Figure 2b. After sintering, a crystallized PZT piezoelectric ceramic skeleton was successfully obtained. The XRD pattern in Figure 2c exhibits distinct diffraction peaks in the 2θ range of 20–60°, corresponding to the (100), (101), (110), (111), (200), (210), and (211) planes of PZT skeleton, confirming that the synthesized PZT possesses a pure perovskite phase. Figure 2d displays the microscopic morphology of the sintered PZT skeleton, revealing a three-dimensional interconnected structure that facilitates efficient stress transfer among grains. Furthermore, EDS elemental mapping confirms the relatively homogeneous distribution of Pb, Zr, Ti, and O within the PZT regions, with no apparent elemental enrichment (Figure 2e–h). The high-magnification SEM image in Figure 2i further reveals a sintered PZT structure composed of closely packed, interconnected grains with an average size of 450 nm. Such a compact and well-ordered grain configuration facilitates effective mechanical load distribution, thereby offering clear microstructural insights into the superior piezoelectric response. The sintered PZT network was coated with PDMS and thermally cured to form the organic–inorganic composite. As shown in Figure 2j, the raised regions correspond to the inorganic component PZT, while the smoother regions indicate the PDMS matrix, suggesting effective infiltration of PDMS into the interstitial spaces and intimate interfacial contact with the ceramic phase. By embedding the brittle PZT architecture within a resilient PDMS medium, the composite achieves exceptional mechanical compliance and fatigue resistance while maintaining robust piezoelectric output, making it highly attractive for wearable sensing platforms.

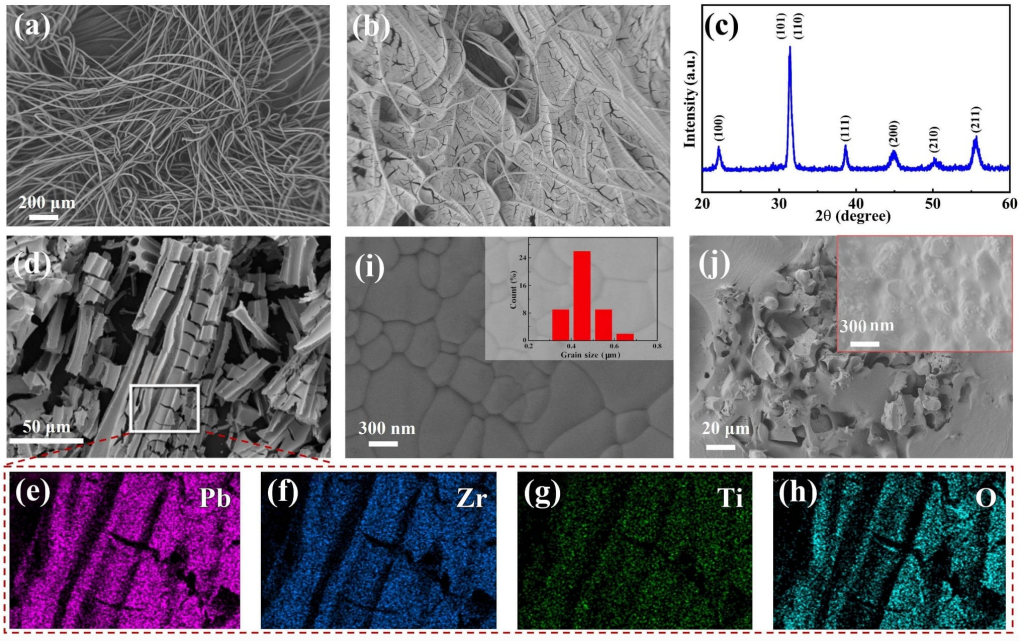

Figure 2. Microscopic morphology, phase composition, and elemental characterization of the PZT and PZT/PDMS composite films. (**a**) SEM image of the microscopic fibers of dust-free paper. (**b**) SEM image of the fibers after immersion in the PZT precursor solution. (**c**) XRD pattern of the PZT. (**d**) SEM image of the PZT structure after pyrolysis, with the corresponding EDS elemental maps of (**e**) Pb, (**f**) Zr, (**g**) Ti, and (**h**) O. (**i**) High-magnification SEM image of the PZT after pyrolysis. (**j**) SEM image of the PZT/PDMS composite.

3.3. Electrical and Energy-Harvesting Performance

To evaluate the dynamic electrical response under mechanical loading, a drop-weight impact system was employed. Individual impacts were applied by releasing 2, 5, 10, and 20 g weights from a height of 30 cm, as illustrated in Figure 3a. The impactor face diameters were 7.00, 8.99, 12.025, and 15.12 mm, respectively. The mechanical force delivered by the impacting ball is determined by the ratio of its momentum variation (Δmgh) to the contact duration (Δt). Assuming complete arrest of the ball upon impact, the transferred momentum is quantified as Δmgh using the mass (m), gravity (g), and drop height (h). The interaction time (Δt) is deduced to be 0.01 s from the pulse width of the device's voltage output (as shown in Figure 3b). Consequently, the output voltages of the PZT-skeleton/PDMS-based FPS under various impact forces are summarized in Figure 3b, yielding a corresponding sensitivity of 4.29 V N^{-1}. Importantly, under identical impact conditions, the polarized PZT-skeleton/PDMS-based FPS generates a substantially higher output voltage than the polarized PZT-powder/PDMS-based FPS, demonstrating enhanced electromechanical transduction resulting from the 3D interconnected piezoelectric skeleton (Figure 3c). In contrast, the unpoled PZT-skeleton/PDMS-based FPS generates no discernible voltage signal, confirming both that the PZT skeleton exhibits no self-polarization and that the output signal of the poled FPS originates from intrinsic piezoelectricity rather than triboelectric or electrostatic artifacts.

Figure 3d schematically illustrates the piezoelectric working mechanism of the PZT-skeleton/PDMS-based FPS. Before poling, the charge dipoles within the PZT-skeleton/PDMS composite are randomly oriented, whereas during poling, they reorient to align with the applied electric field (Figure 3(dI)). Upon compression, the decreased interelectrode distance reduces the electric dipole moments. The resulting piezoelectric potential drives free electrons through the external circuit from the negative electrode to the positive electrode (Figure 3(dII)). Upon removal of the compressive force, the recovery of the composite

deformation restores the charge dipole moments and increases the internal polarization. The change in polarization induces a redistribution of surface charges, causing electrons to migrate from the positive electrode back to the negative electrode (Figure 3(dIII)). Accordingly, the FPS produces electrical signals with alternating polarities under successive loading and unloading cycles.

The measured highest piezoelectric coefficient (d_{33}) of the FPS reaches 34 pC/N (as shown in Figure 3e), which significantly exceeds the values reported for devices with randomly dispersed inorganic phases within an organic matrix, further highlighting the prominent advantages of the 3D interconnected PZT skeleton in boosting electromechanical conversion (Figure 3e) [35]. To rigorously verify that the generated voltage signals genuinely originate from the intrinsic piezoelectric effect of PZT, a polarity-switching test was performed (Figure 3f). The observed phase reversal of the voltage signals under reverse connection conclusively rules out triboelectric or capacitive interference. In addition to its exceptional electromechanical conversion capability, the sensor demonstrates outstanding mechanical durability, retaining approximately 80% of its initial output voltage after 10^6 mechanical loading cycles (Figure 3g), which strongly demonstrates its remarkable fatigue resistance. The dependence of the output voltage on various bending angles was also systematically investigated. As the bending angle increased from 30° to 90°, the output voltage rose correspondingly from 4 V to 11 V, highlighting a pronounced deformation-dependent response (Figure 3h). Moreover, the device demonstrates excellent mechanical robustness and deformation stability, showing consistent and reliable voltage signal over 1000 bending–releasing cycles at a fixed angle of 60° (Figure 3i).

In addition to its direct voltage response under mechanical loading, the electrical output characteristics of the device under different load resistances were examined [36]. As shown in Figure 3j, the output voltage increased with load resistance and gradually plateaued, whereas the output power peaked (calculated according to the formula $P = V^2/R$, where V denotes the output voltage and R represents the load resistance) at approximately 23 μW at 5 MΩ before declining, identifying the optimal load resistance for power generation. The energy-harvesting capability was further demonstrated using a four-diode full-wave bridge rectifier to drive a green LED (see the inset of Figure 3k). These results confirm the device's energy-conversion capability and motivate its evaluation under practical mechanical stimuli.

3.4. Application

To evaluate the practical utility of the PZT-skeleton/PDMS-based FPS in human-activity monitoring, the sensor was attached to various body parts to record dynamic physiological movements. As shown in Figure 4a–d, the device responds to four representative mechanical stimuli: finger pressing, hand tapping, hammer impact, and foot stepping, producing peak voltages of approximately 10, 19.6, 26.4, and 17.6 V, respectively. The distinct outputs reflect differences in applied force, contact mode, and deformation, demonstrating the device's potential for real-time health and activity monitoring. Hammer impact produced the highest voltage, reflecting enhanced deformation of the PZT/PDMS composite under stronger mechanical excitation. These results demonstrate the device's ability to respond to diverse mechanical stimuli, consistent with research on conformable on-body piezoelectric energy harvesters and self-powered wearable sensors [5,6].

The device was further used to detect repetitive, localized stimuli during mouse clicking and keyboard typing (Figure 4e,f). Mouse clicks generated a peak voltage of approximately 7 V, while keyboard typing produced 4.4 V. The distinct, periodic voltage pulses reflect differences in force and contact conditions, enabling mouse clicks and keystrokes to be identified by pulse counting. These results demonstrate that the device converts low-

frequency, repetitive mechanical inputs into detectable electrical signals, enabling simple identification of routine human–computer interactions.

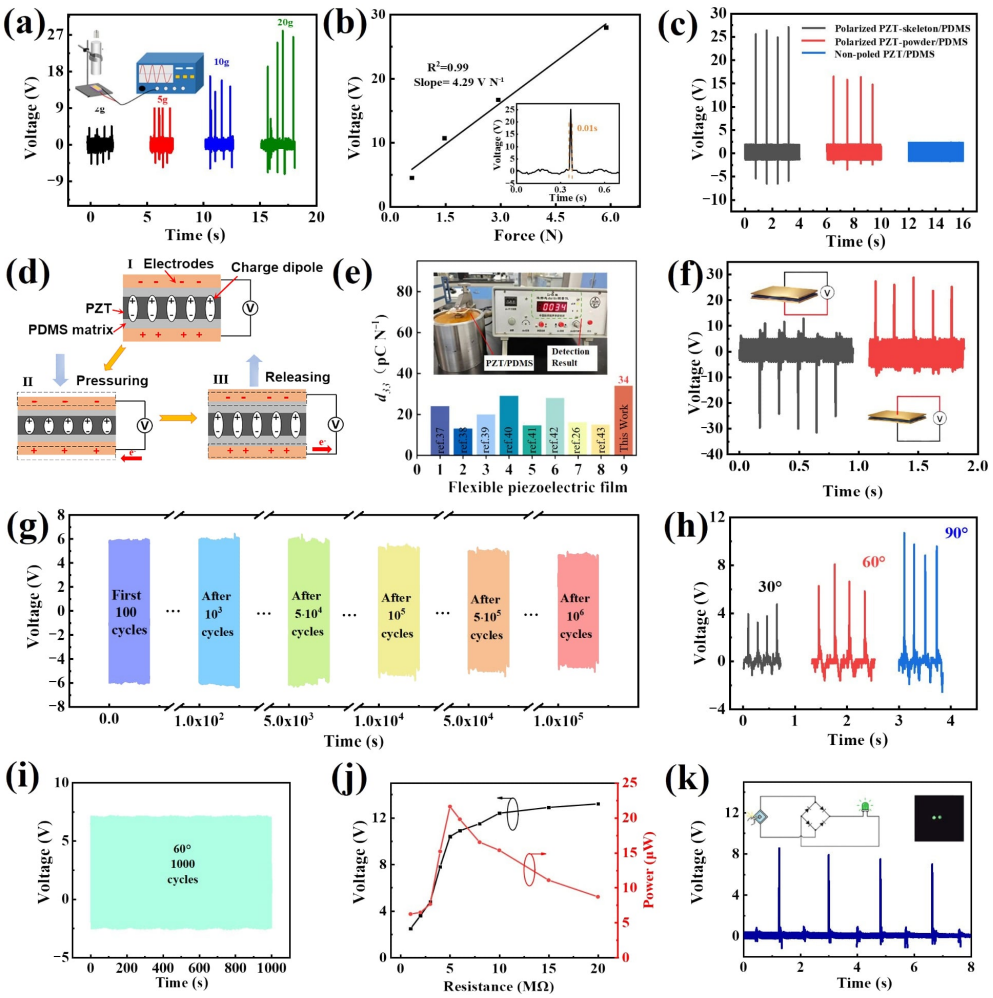

Figure 3. Electrical and energy-harvesting performance of the PZT/PDMS flexible piezoelectric device. (**a**) Output voltages under different impact masses; inset: testing setup. (**b**) Output voltage versus force; inset: transient voltage response. (**c**) Comparison of the output voltage of the FPS among polarized PZT-skeleton/PDMS, polarized PZT-powder/PDMS, and unpolarized PZT-skeleton/PDMS. (**d**) Schematic illustration of the piezoelectric working mechanism, showing (**I**) the initial unloaded state, (**II**) compression and charge redistribution, and (**III**) unloading and recovery. (**e**) Comparison of d_{33} values with representative flexible piezoelectric films [26,37–43]; inset: measurement setup. (**f**) Voltage responses under normal and reversed electrical connections. (**g**) Cyclic loading stability over 10^6 cycles. (**h**) Voltage responses at different bending angles. (**i**) Output stability during 1000 bending cycles at 60°. (**j**) Output voltage and peak power versus load resistance. (**k**) Rectified voltage output; insets: rectifier circuit and LED illumination.

Beyond human motion and device operation, the FPS was evaluated for detecting fluid-induced mechanical disturbances, as shown in Figure 4g. The output voltage was approximately 15 mV with the faucet closed, increased to approximately 55 mV when the faucet was fully opened, and returned to approximately 10 mV after closure. These findings confirm that the sensor can effectively capture subtle micro-vibrations generated by water flow, enabling real-time monitoring of water supply states (e.g., normal flow and pipeline blockage) across diverse, complex pipe geometries.

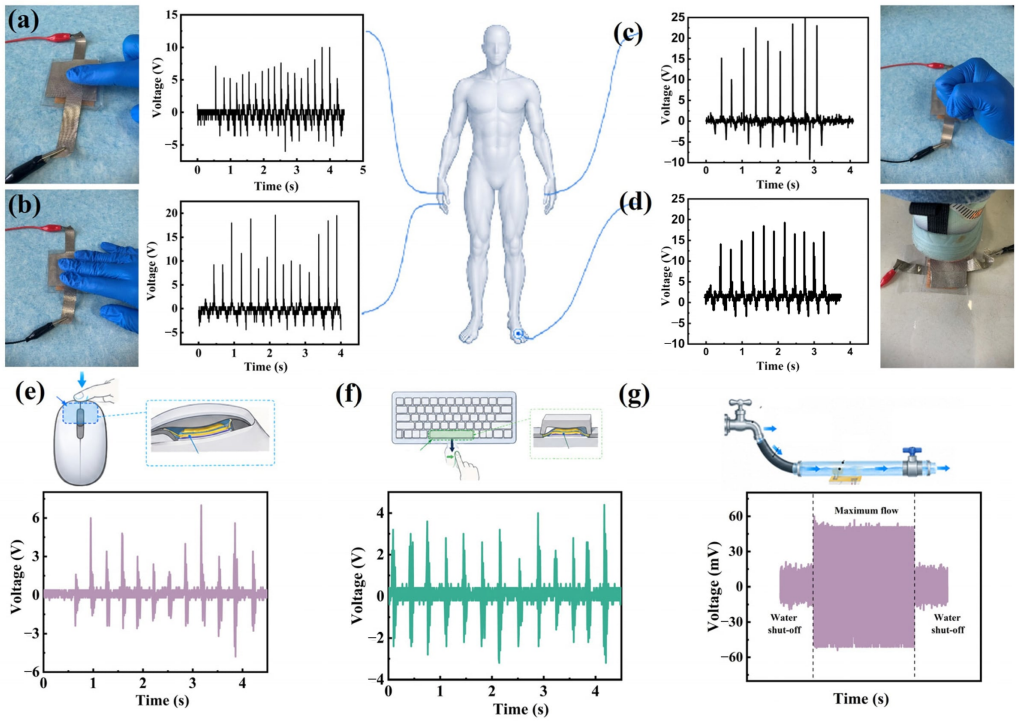

Figure 4. Response characteristics and practical applications of the flexible PZT/PDMS piezoelectric device: (**a**–**d**) Electrical responses to finger pressing, hand tapping, hammer impact, and foot stepping, respectively. (**e**,**f**) Mouse-clicking and keyboard-typing detection, respectively. (**g**) Experimental setup and voltage response during qualitative detection of flow-induced mechanical disturbances in a rubber tube. The central human-body schematic was generated using ChatGPT (GPT-5.6 Sol, OpenAI) and reviewed and edited by the authors.

Given that the sacrificial templating strategy combined with mold-assisted sintering enables the fabrication of large-area PZT piezoelectric ceramic skeleton, we further explored a piezoelectric sensing array based on this configuration. As shown in Figure 5a, symmetrical electrodes were sputter-deposited on both surfaces of the PZT-skeleton/PDMS composite, and each element was individually poled in sequence to prevent signal interference among the piezoelectric units. To verify the independence of each piezoelectric unit, mechanical pressure was sequentially applied to Elements 1–3. When Element 1 was subjected to physical pressure, no discernible voltage response was detected in the adjacent Elements 2 and 3 (Figure 5b). Similarly, when either Element 2 or 3 was actuated, no discernible voltage responses were detected in the neighboring elements, demonstrating excellent channel independence. The spatial pressure-sensing capability was further demonstrated by placing a strip-shaped object across the sensor array. Upon applying pressure with an elongated block onto the sensor array, the contacted sensing units exhibited significantly elevated voltage outputs compared to the unloaded units (Figure 5c). This spatially dependent output demonstrates that the array can map the distribution of applied pressure and distinguish variations in contact position.

This superior spatial mapping capability of the sensor array prompted us to further evaluate its suitability as wearable electronics for motion tracking, such as gait monitoring [44,45]. The sensor was attached beneath the sole of a shoe to characterize plantar pressure distributions under different foot orientations. Figure 5d–f present the voltage distributions associated with out-toeing, normal, and in-toeing gait patterns, respectively. During out-toeing, the voltage responses were higher in the lateral regions, indicating a greater load on the outer side of the foot. Under normal gait conditions, the responses were comparatively more evenly distributed across the sensing regions, suggesting a more

balanced plantar loading pattern. In contrast, during in-toeing, stronger responses were observed in the medial regions, consistent with increased loading on the inner side of the foot. These distinct spatial response patterns demonstrate the capability of the sensor array to differentiate diverse gait-induced plantar pressure distributions. This capability empowers real-time movement monitoring and posture rehabilitation, thereby paving a vital way for the development of advanced flexible medical electronics.

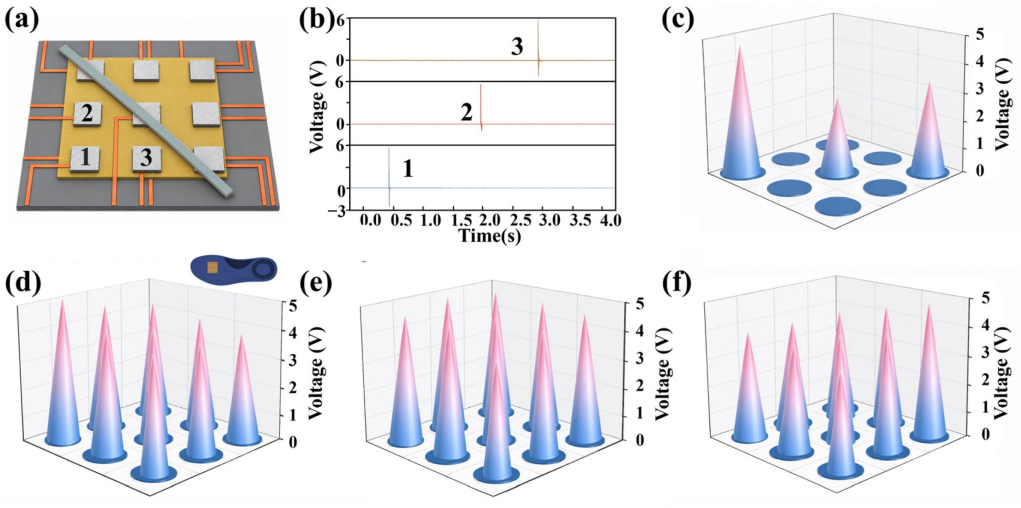

Figure 5. Spatial pressure mapping and gait monitoring using the flexible PZT/PDMS sensor array. (**a**) Schematic illustration of the 3 × 3 sensing configurations formed by individually polarized regions on a common PZT substrate, with regions 1–3 highlighted for electrical response testing. (**b**) Voltage–time curves recorded during sequential stimulation of regions 1, 2, and 3. (**c**) Three-dimensional voltage distribution under loading by a strip-shaped object. (**d**–**f**) Three-dimensional voltage distribution maps under different gait patterns: (**d**) out-toeing, (**e**) normal gait, and (**f**) in-toeing. In (**c**–**f**), cone heights represent peak output voltages, while the blue-to-pink shading is used for visualization.

4. Conclusions

In summary, a flexible PZT/PDMS composite featuring a continuous ceramic network was successfully fabricated via a sacrificial dust-free paper template combined with mold-assisted sintering, thereby synergistically integrating the high piezoelectric activity of PZT with the mechanical compliance of PDMS. The composite exhibits a d_{33} of 34 pC/N, an output voltage of up to 28 V under mechanical impact. After 10^6 loading cycles, it retains approximately 80% of its initial output voltage. Furthermore, a 3 × 3 electrode configuration enables spatially resolved detection of localized mechanical stimuli across the continuous film. Responses to human motion, keyboard operation, and water flow further demonstrate its versatility in detecting diverse mechanical disturbances. This work highlights continuous ceramic-network design as a practical approach to flexible piezoelectric composites for wearable sensing and spatially distributed mechanical monitoring.

Author Contributions: Writing—original draft preparation, S.J.; methodology and investigation, X.Y.; software, J.X.; validation, M.L.; supervision, funding acquisition, and writing—review and editing, C.Y. All authors have read and agreed to the published version of the manuscript.

Funding: This work was supported by the Shandong Province Key Fundamental Research Program (Grant No. ZR2026ZD42), Interdisciplinary Convergence Construction Project of the University of Jinan (XKJC-202401, XKJC-202511), the University of Jinan Major Science and Technology Projects and Landmark Achievements Cultivation Program (XKY2508).

Data Availability Statement: The original contributions presented in this study are included in the article. Further inquiries can be directed to the corresponding author.

Acknowledgments: During the preparation of this manuscript, the authors used ChatGPT's image-generation tool (OpenAI), accessed through ChatGPT 6 Sol, to generate the device schematic in Figure 1d using a photograph of the assembled device as a reference. The prompt specified the layered arrangement of the PI tape, copper electrodes, and PZT/PDMS composite and placed each silver-paste joint between its copper electrode and the adjacent PI tape. The generated schematic depicts the device architecture and electrical connections. The authors also used ChatGPT (GPT-5.6 Sol, OpenAI) to generate the schematic of the human body shown in the center of Figure 4. The authors reviewed and edited the generated content and take full responsibility for the content of this publication.

Conflicts of Interest: The authors declare no conflicts of interest.

References

1. Chen, Y.; Zhang, X.; Lu, C. Flexible Piezoelectric Materials and Strain Sensors for Wearable Electronics and Artificial Intelligence Applications. *Chem. Sci.* **2024**, *15*, 16436–16466. [CrossRef] [PubMed]
2. Su, D.; Jiang, L.; Pan, Z.; Yang, C.; Liu, C.; Liu, R.; Liu, T.; He, X.; Huang, S.; Cheng, Z. Ultrasensitive, Signal-Complementary Piezo-Capacitive Pressure Sensor for Complex Physiological Monitoring and HMI. *Chem. Eng. J.* **2025**, *526*, 170883. [CrossRef]
3. Wang, X.; Yu, J.; Cui, Y.; Li, W. Research Progress of Flexible Wearable Pressure Sensors. *Sens. Actuators A Phys.* **2021**, *330*, 112838. [CrossRef]
4. Cui, X.; Huang, F.; Zhang, X.; Song, P.; Zheng, H.; Chevali, V.; Wang, H.; Xu, Z. Flexible Pressure Sensors via Engineering Microstructures for Wearable Human-Machine Interaction and Health Monitoring Applications. *iScience* **2022**, *25*, 104148. [CrossRef] [PubMed]
5. Wang, Y.; Yu, Y.; Wei, X.; Narita, F. Self-Powered Wearable Piezoelectric Monitoring of Human Motion and Physiological Signals for the Postpandemic Era: A Review. *Adv. Mater. Technol.* **2022**, *7*, 2200318. [CrossRef]
6. Fernandez, S.V.; Cai, F.; Chen, S.; Suh, E.; Tiepelt, J.; McIntosh, R.; Marcus, C.; Acosta, D.; Mejorado, D.; Dagdeviren, C. On-Body Piezoelectric Energy Harvesters through Innovative Designs and Conformable Structures. *ACS Biomater. Sci. Eng.* **2023**, *9*, 2070–2086. [CrossRef] [PubMed]
7. Persano, L.; Dagdeviren, C.; Su, Y.; Zhang, Y.; Girardo, S.; Pisignano, D.; Huang, Y.; Rogers, J.A. High Performance Piezoelectric Devices Based on Aligned Arrays of Nanofibers of Poly(vinylidenefluoride-co-trifluoroethylene). *Nat. Commun.* **2013**, *4*, 1633. [CrossRef] [PubMed]
8. Tang, J.; Li, Y.; Yu, Y.; Hu, Q.; Du, W.; Lin, D. Recent Progress in Flexible Piezoelectric Tactile Sensors: Materials, Structures, Fabrication, and Application. *Sensors* **2025**, *25*, 964. [CrossRef] [PubMed]
9. Bouhamed, A.; Missaoui, S.; Ben Ayed, A.; Attaoui, A.; Missaoui, D.; Jeder, K.; Guesmi, N.; Njeh, A.; Khemakhem, H.; Kanoun, O. A Comprehensive Review of Strategies toward Efficient Flexible Piezoelectric Polymer Composites Based on $BaTiO_3$ for Next-Generation Energy Harvesting. *Energies* **2024**, *17*, 4066. [CrossRef]
10. Zhao, T.; Li, J.; Yang, X.; Yin, Z. A Review of the Preparation and Application of Lead Zirconate Titanate (PZT) Thin Film Sensors. *J. Mater. Chem. C* **2025**, *13*, 15807–15851. [CrossRef]
11. Lv, P.; Qian, J.; Yang, C.; Liu, T.; Wang, Y.; Wang, D.; Huang, S.; Cheng, X.; Cheng, Z. Flexible All-Inorganic Sm-Doped PMN-PT Film with Ultrahigh Piezoelectric Coefficient for Mechanical Energy Harvesting, Motion Sensing, and Human-Machine Interaction. *Nano Energy* **2022**, *97*, 107182. [CrossRef]
12. He, S.; Dong, W.; Guo, Y.; Guan, L.; Xiao, H.; Liu, H. Piezoelectric Thin Film on Glass Fiber Fabric with Structural Hierarchy: An Approach to High-Performance, Superflexible, Cost-Effective, and Large-Scale Nanogenerators. *Nano Energy* **2019**, *59*, 745–753. [CrossRef]
13. Sekhar, M.C.; Veena, E.; Kumar, N.S.; Naidu, K.C.B.; Mallikarjuna, A.; Basha, D.B. A Review on Piezoelectric Materials and Their Applications. *Cryst. Res. Technol.* **2023**, *58*, 2200130. [CrossRef]
14. Zhen, L.; Lu, L.; Yao, Y.; Liu, J.; Yang, B. Flexible Inorganic Piezoelectric Functional Films and Their Applications. *J. Adv. Ceram.* **2023**, *12*, 433–462. [CrossRef]
15. Xie, M.; Zhang, Y.; Kraśny, M.J.; Bowen, C.R.; Khanbareh, H.; Gathercole, N. Flexible and Active Self-Powered Pressure, Shear Sensors Based on Freeze Casting Ceramic–Polymer Composites. *Energy Environ. Sci.* **2018**, *11*, 2919–2927. [CrossRef] [PubMed]
16. Newnham, R.E.; Skinner, D.P.; Cross, L.E. Connectivity and Piezoelectric-Pyroelectric Composites. *Mater. Res. Bull.* **1978**, *13*, 525–536. [CrossRef]

17. Chamankar, N.; Khajavi, R.; Yousefi, A.A.; Rashidi, A.; Golestanifard, F. An Experimental Model for Predicting the Piezo and Dielectric Constant of PVDF-PZT Nanocomposite Fibers with 0–3 and 1–3 Connectivity. *Ceram. Int.* **2020**, *46*, 23567–23581. [CrossRef]
18. Babu, I.; de With, G. Highly Flexible Piezoelectric 0–3 PZT–PDMS Composites with High Filler Content. *Compos. Sci. Technol.* **2014**, *91*, 91–97. [CrossRef]
19. D'Ambrogio, G.; Zahhaf, O.; Le, M.-Q.; Capsal, J.-F.; Cottinet, P.-J. Dielectrophoresis Structurization of PZT/PDMS Micro-Composite for Elastronic Function: Towards Dielectric and Piezoelectric Enhancement. *Materials* **2021**, *14*, 4071. [CrossRef] [PubMed]
20. Meyer, Y.; Lachat, R.; Akhras, G. A Review of Manufacturing Techniques of Smart Composite Structures with Embedded Bulk Piezoelectric Transducers. *Smart Mater. Struct.* **2019**, *28*, 053001. [CrossRef]
21. Selleri, G.; Gino, M.E.; Zonzini, F.; De Marchi, L.; Focarete, M.L.; Fabiani, D.; Zucchelli, A.; Brugo, T.M. PZT Piezoceramic Nanofibers for Impact Localization in Composite Laminates. *Thin-Walled Struct.* **2026**, *218*, 114104. [CrossRef]
22. Zhang, G.; Zhao, P.; Zhang, X.; Han, K.; Zhao, T.; Zhang, Y.; Jeong, C.K.; Jiang, S.; Zhang, S.; Wang, Q. Flexible Three-Dimensional Interconnected Piezoelectric Ceramic Foam Based Composites for Highly Efficient Concurrent Mechanical and Thermal Energy Harvesting. *Energy Environ. Sci.* **2018**, *11*, 2046–2056. [CrossRef]
23. Feng, X.; Xu, J.; Zhang, K.; Xia, C.; Gao, X.; Zheng, M.; Hou, Y.; Gao, F.; Zhang, S. High-Sensitivity Piezoelectric Response Enabled by Heterogeneous Stress–Electric Field Distribution in 3D Interconnected Porous Ceramics. *J. Adv. Ceram.* **2026**, *15*, 9221280. [CrossRef]
24. Hong, Y.; Wang, B.; Long, Z.; Zhang, Z.; Pan, Q.; Liu, S.; Luo, X.; Yang, Z. Hierarchically Interconnected Piezoceramic Textile with a Balanced Performance in Piezoelectricity, Flexibility, Toughness, and Air Permeability. *Adv. Funct. Mater.* **2021**, *31*, 2104737. [CrossRef]
25. Yin, H.; Li, Y.; Tian, Z.; Li, Q.; Jiang, C.; Liang, E.; Guo, Y. Ultra-High Sensitivity Anisotropic Piezoelectric Sensors for Structural Health Monitoring and Robotic Perception. *Nano-Micro Lett.* **2025**, *17*, 42. [CrossRef] [PubMed]
26. Xu, Z.; Li, C.; Wang, S.; Lv, Q.; Zou, S.; Xu, J.; Dong, T.; Wang, J.; Li, X.; Su, D.; et al. Multiscale Interconnected Lead-Free Piezoceramic Skeleton-Based Flexible Piezoelectric Sensors for Wearable Electronics and Energy Harvesting. *J. Mater. Sci. Mater. Electron.* **2026**, *37*, 1713. [CrossRef]
27. Lin, X.; Zhang, X.; Fei, X.; Wang, C.; Liu, H.; Huang, S. Flexible Three-Dimensional Interconnected PZT Skeleton Based Piezoelectric Nanogenerator for Energy Harvesting. *Ceram. Int.* **2023**, *49*, 27526–27534. [CrossRef]
28. Xiao, Y.; Yang, L.; Zhang, M.; Li, X.; Xu, E.; Yang, M.; Hu, P.; Shen, Y. Ultrahigh Piezoelectric Performances in Soft Lead Zirconate Titanate/Polydimethylsiloxane Composites by Ethanol-Assisted Freeze Casting. *Nat. Commun.* **2026**, *17*, 6957. [CrossRef] [PubMed]
29. Xu, J.; Shao, Y.; Feng, X.; Zhang, X.; Li, H.; Yang, J.; Gao, F. Low Sintering Shrinkage Porous Ceramics: Principles, Progress, and Perspectives. *J. Adv. Ceram.* **2025**, *14*, 9221015. [CrossRef]
30. Lin, W.; Wang, B.; Peng, G.; Shan, Y.; Hu, H.; Yang, Z. Skin-Inspired Piezoelectric Tactile Sensor Array with Crosstalk-Free Row+Column Electrodes for Spatiotemporally Distinguishing Diverse Stimuli. *Adv. Sci.* **2021**, *8*, 2002817. [CrossRef] [PubMed]
31. Xu, Q.; Wang, Z.; Zhong, J.; Yan, M.; Zhao, S.; Gong, J.; Feng, K.; Zhang, J.; Zhou, K.; Xie, J.; et al. Construction of Flexible Piezoceramic Array with Ultrahigh Piezoelectricity via a Hierarchical Design Strategy. *Adv. Funct. Mater.* **2023**, *33*, 2304402. [CrossRef]
32. Li, J.; Ding, W.; Yang, D.; Huang, Z.; Wang, H.; Feng, P.; Ran, Q.; Wang, Z. Flexible P(VDF-TrFE) Piezoelectric Sensor Array with Low Signal Crosstalk for Dynamic Impulse Stress Recognition. *Sens. Actuators A Phys.* **2026**, *407*, 117933. [CrossRef]
33. Kimberly-Clark Professional. Certificate of Conformance: KIMTECH PURE W5 Wipers (06179/7659). Available online: https://digitalassets.avantorsciences.com/adaptivemedia/rendition?clid=SAPDAM&id=569cfc1be7042465fc411dd9c32b01fae903d54f&prid=original&vid=e652a44003c09a118f3e190d3d053d522aba73db (accessed on 17 November 2026).
34. Dow. SYLGARD™ 184 Silicone Elastomer Kit. Available online: https://www.dow.com/en-us/pdp.sylgard-184-silicone-elastomer-kit.01064291z.html (accessed on 17 November 2026).
35. Šutka, A.; Sherrell, P.C.; Shepelin, N.A.; Lapčinskis, L.; Mālnieks, K.; Ellis, A.V. Measuring Piezoelectric Output—Fact or Friction? *Adv. Mater.* **2020**, *32*, 2002979, Correction in *Adv. Mater.* **2020**, *33*, 2105662. [CrossRef] [PubMed]
36. Jabbar, H.; Jung, H.J.; Chen, N.; Cho, D.H.; Sung, T.H. Piezoelectric Energy Harvester Impedance Matching Using a Piezoelectric Transformer. *Sens. Actuators A Phys.* **2017**, *264*, 141–150. [CrossRef]
37. Zhang, X.F.; Xia, W.M.; Ping, Y.F.; Wang, R.; Wei, T.; Xing, J. Dielectric, Ferroelectric, and Energy Conversion Properties of a KNN/P(VDF-TrFE) Composite Film. *J. Mater. Sci. Mater. Electron.* **2022**, *33*, 12941–12952. [CrossRef]
38. Wei, L.-Z.; Zhang, C.-S.; Wang, C.; Wang, R.-P. The Preparation of PVDF-BTO Composite Film and the Influence of Polarization Intensity on the Piezoelectric Properties of Composite Film. *J. Phys. Conf. Ser.* **2021**, *1948*, 012191. [CrossRef]
39. Li, X.; Yuan, C.; Zhou, H.; Gao, G.; He, J.; Liu, X.; Li, Y.; Sun, H.; Liu, X. A Novel PZT Hollow Structure Utilized in High-Performance Piezoelectric Nanogenerator. *Ceram. Int.* **2024**, *50*, 34756–34767. [CrossRef]

40. Yuan, C.; Li, X.; Yang, X.; Wu, F.; Zhou, H.; Gao, G.; Sun, H.; Liu, X. Application of Multi-Layered Composite Fiber Films with Enhanced Piezoelectric Performance in Flexible Energy Harvesting Devices. *Ceram. Int.* **2024**, *50*, 28735–28745. [CrossRef]
41. Le, J.; Lv, F.; Lin, J.; Wu, Y.; Ren, Z.; Zhang, Q.; Dong, S.; Luo, J.; Shi, J.; Chen, R.; et al. Novel Sandwich-Structured Flexible Composite Films with Enhanced Piezoelectric Performance. *ACS Appl. Mater. Interfaces* **2024**, *16*, 1492–1501. [CrossRef] [PubMed]
42. Yang, X.; Li, Y.; Guo, H.; Xiao, S.; Yuan, C.; Zhang, C.; Sun, H. Efficient Energy Harvesting Enabled by Large-Area Piezoelectric PVDF-Based Composite Film Enhanced by Carbon Nanotubes. *Ceram. Int.* **2024**, *50*, 12185–12194. [CrossRef]
43. Pickwell, A.J.; Smith, A.; Jones, P.M.; Mba, D.; Dorey, R.A. ZnO Surface Modified PZT for Enhanced Ceramic Composite Thick Film Sensors. *Adv. Appl. Ceram.* **2013**, *112*, 283–287. [CrossRef]
44. Cha, Y.; Kim, H.; Kim, D. Flexible Piezoelectric Sensor-Based Gait Recognition. *Sensors* **2018**, *18*, 468. [CrossRef] [PubMed]
45. Han, S.; Xiao, Q.; Liang, Y.; Chen, Y.; Yan, F.; Chen, H.; Yue, J.; Tian, X.; Xiong, Y. Using Flexible-Printed Piezoelectric Sensor Arrays to Measure Plantar Pressure during Walking for Sarcopenia Screening. *Sensors* **2024**, *24*, 5189. [CrossRef] [PubMed]

Disclaimer/Publisher's Note: The statements, opinions and data contained in all publications are solely those of the individual author(s) and contributor(s) and not of MDPI and/or the editor(s). MDPI and/or the editor(s) disclaim responsibility for any injury to people or property resulting from any ideas, methods, instructions or products referred to in the content.